

Simultaneous micro-PIV measurements and real-time control trapping in a cross-slot channel

Farzan Akbaridoust¹  · Jimmy Philip¹ · David R. A. Hill² · Ivan Marusic¹

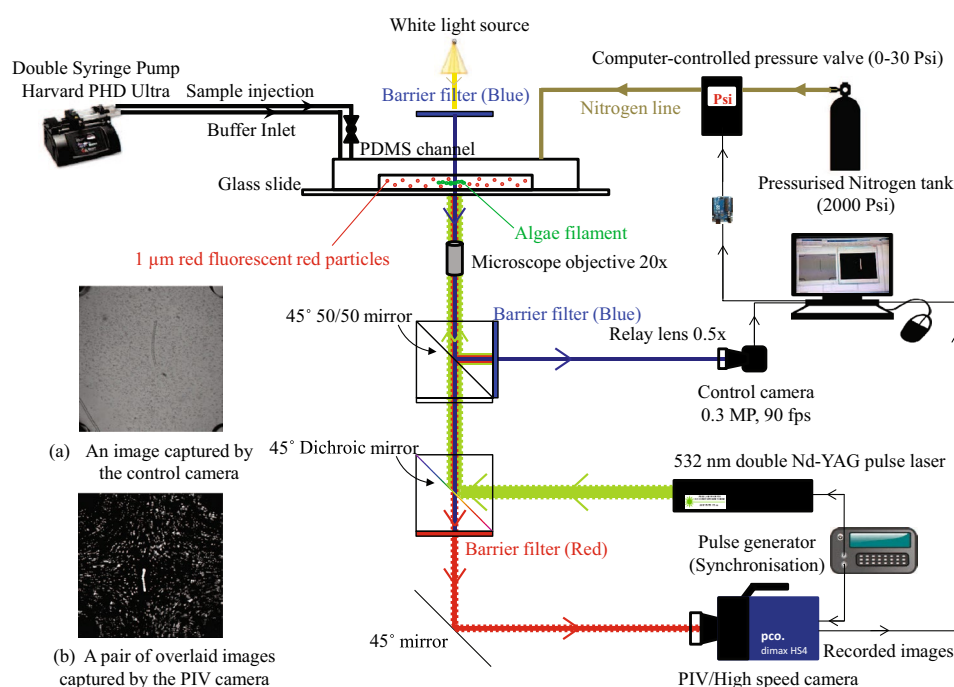
Abstract

Here we report novel micro-PIV measurements around micron-sized objects that are trapped at the centre of a stagnation point flow generated in a cross-slot microchannel using real-time control. The method enables one to obtain accurate velocity and strain rate fields around the trapped objects under straining flows. In previous works, it has been assumed that the flow field measured in the absence of the object is the one experienced by the object in the stagnation point flow. However, the results reveal that this need not be the case and typically the strain rates experienced by the objects are higher. Therefore, simultaneously measuring the flow field around a trapped object is needed to accurately estimate the undisturbed strain rate (away from the trapped object). By combining the micro-PIV measurements with an analytical solution by Jeffery (Proc R Soc Lond A 102(715):161–179, 1922), we are able to estimate the velocity and strain rate around the trapped object, thus providing a potential fluidic method for characterising mechanical properties of micron-sized materials, which are important in biological and other applications.

Graphical abstract

Electronic supplementary material The online version of this article (<https://doi.org/10.1007/s00348-018-2637-6>) contains supplementary material, which is available to authorized users.

Extended author information available on the last page of the article



Schematic of the modified simultaneous micro-PIV and control experimental setups.

A novel combination of classical micro-PIV and real-time flow control setups enabled us to measure the velocity field around a target trapped in the extensional flow, which opens up new vistas of characterisation of the mechanical properties of micron-sized objects.

1 Introduction

Hydrodynamic-based microfluidic traps have been widely used to confine and manipulate micron-sized objects in an extensional (stagnation point) flow in cross-slot microchannels. This microfluidic platform is used as a valuable tool in the fields of biology and engineering to carry out single-cell analysis and study the dynamics of other micron-sized objects (Johnson-Chavarria et al. 2011, 2014; Tanyeri and Schroeder 2018; Tanyeri et al. 2010, 2011). Typically, there are two aspects of the hydrodynamic-based microfluidic trap; first, to control and trap the micron-sized objects in the flow, and second, the characterisations of the flow itself are studied separately. For trapping, the conventional method involves using a video camera that monitors a micron-sized object in the microfluidic device and adjusting pressure in an on-chip membrane valve as a feedback loop to ensure that the object remains trapped at the zero-velocity (stagnation) point of the extensional flow (Tanyeri et al. 2010). The flow characterisation, the other aspect of the platform, is carried out by numerical simulation or using micron-resolution particle image velocimetry (micro-PIV) measurements of the flow inside the microfluidic device, however, with the object

absent. In fact, simultaneous trapping of objects and velocity measurements is challenging because both require their own illumination, optics and camera focused on the micron-sized objects. Consequently, it is usually assumed that the flow field measured in the absence of the object is the one experienced by the object, though this need not be the case depending on the object size relative to the channel dimensions. Most of the efforts on this type of trap have concentrated on improving the ability to confine the objects, which include increasing the trap stiffness and residence time and they have relied on the flow characteristics of the extensional flow with the absence of the target objects. However, in this study, we develop a unique method that enables one to obtain the flow characteristics in real time while a single target is trapped in the flow. This enables one to calculate more precise information regarding the flow parameters including the strain rate experienced by the trapped objects. We find that trapped objects change the flow. As such, velocity field measured in the absence of the object may not represent the correct flow field in the microfluidic device.

Over the last two decades, advances in microfluidic technology have enabled researchers to trap and immobilise nano- and micron-sized objects such as single

micro-particles, cells and macro-DNA molecules using different types of microfluidic traps such as magnetic (Gosse and Croquette 2002; Lee et al. 2004), optical (Ashkin et al. 1986; Grier 2003; Yang et al. 2009), acoustic (Bernassau et al. 2014; Hertz 1995; Qiu et al. 2014) and hydrodynamic traps (Tanyeri et al. 2010, 2011). Amongst the traps mentioned, the hydrodynamic trap solely utilises hydrodynamic forces for confinement of a micron-sized object in a flow, whereas the others are dependent on external forces such as magnetic, acoustic and optical. Therefore, a hydrodynamic trap is the best option to conduct micro-biological experiments when similarity of the flow to their natural habitat is required.

The first hydrodynamic trap was in a four-roll mill (Taylor 1934), which is suitable for trapping millimetre-sized objects. It is not a suitable platform for confining micron-sized objects due to the difficulty of maintaining a fixed location of the stagnation point within one micron (Akbari-doust et al. 2018).

Another apparatus that can produce the same type of flow as Taylor's four-roll mill is a cross-slot channel (schematically shown in Fig. 1). Cross-slot channels consist of two co-linear converging inlets, and two diverging outlet laminar streams orthogonal to the inlet flows. The two inlet laminar flows meet at the intersection of the cross-junction, where a two-dimensional extensional flow with a zero-velocity (stagnation) point and hyperbolic streamlines are generated. The velocity equations of a pure stagnation point flow are given by $u = \gamma x$, $v = -\gamma y$, where γ is the strain rate of the flow. Ideal straining stagnation point flow has hyperbolic streamlines ($xy = \text{const.}$) and spatially uniform strain rate ($\gamma = \text{const.}$).

1.1 Trapping of objects in cross-slot microchannel

In the 1990s, with the emergence of microfluidic devices, cross-slot microchannels were used to trap micron-sized objects such as DNA molecules in a stagnation point flow. However, this was limited to short-term confinement of the target (Perkins et al. 1997) as the stagnation point is a semi-equilibrium stable point (Tanyeri et al. 2010). Later, relatively longer confinement of single objects was achieved using human-facilitated control systems in cross-slot microchannels

(Dylla-Spears et al. 2010; Schroeder et al. 2003, 2004; Xu and Muller 2011).

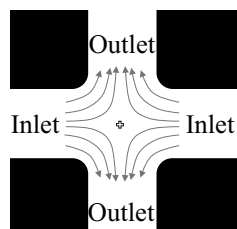
Over the last several years, using an image-based active control system, long-term trapping of a single micron-sized object became possible. Schroeder and co-workers (Johnson-Chavarria et al. 2011, 2014; Latinwo et al. 2014; Li et al. 2015; Shenoy et al. 2015; Tanyeri and Schroeder; Tanyeri et al. 2010, 2011) developed an image-based microfluidic hydrodynamic trap in the straining flow of a cross-slot microchannel for high-resolution confinement of single micron-sized objects. To tackle the Brownian motion and to achieve long-term confinement of micron-sized beads, Tanyeri et al. (2010) implemented an on-chip membrane valve (filled with a pressurised gas) on one of the outlets of the cross-junction of the microfluidic device to control the position of the stagnation point. Johnson-Chavarria et al. (2011) demonstrated the fabrication of the double-layer microfluidic device used in this type of microfluidic trap and visualised how to operate the trap. Tanyeri et al. (2011) comprehensively presented the design and implementation of the controlled hydrodynamic trap and characterised the effect of various parameters used in fabrication of the microfluidic device and the dimensions of the device on the time response of the membrane valve. Curtis et al. (2011) simulated the flow and the control system in a cross-slot microfluidic device with a considerably lower computational cost in comparison with conventional simulations to propose an apparatus for cell sorting. Johnson-Chavarria et al. (2014) used an adaptive control algorithm to achieve longer trapping and they confined an *Escherichia coli* cell, to investigate the effect of cell growth environment by observation of the cell growth dynamics, intracellular diffusion proteins and gene expression. The same basic concepts of the trapping were used by Shenoy et al. (2016), in a microfluidic device with more inlets and outlets to produce a double-stagnation point flow to simultaneously trap multiplexed particle manipulation (called a Stokes trap).

Recently, cross-slot microfluidic devices were used as means of single-cell mechanophenotyping (Cha et al. 2012; Gossett et al. 2012; Henon et al. 2014; Henry et al. 2013). For a high throughput of 2000 cell/s, Gossett et al. (2012) and Henry et al. (2013) applied very high strain rates (about 10^5 s^{-1}). Using an inertial focusing technique and a high-speed camera, they observed and characterised the cell deformability at the cross-slot junction. However, the residence time of the sample was $O(10^{-5} \text{ s})$. The method is, therefore, not suitable for long-term straining flow exposure to target objects.

1.2 Velocity measurements in cross-slot microchannel

Researchers have measured the velocity field by either tracking a few particles (Tanyeri et al. 2010), or to acquire more precise

Fig. 1 Schematic of a cross-slot channel



results, others have measured velocity and strain rate fields using micro-PIV (Akbaridoust 2017; Akbaridoust et al. 2018; Alicia et al. 2016; Pathak and Hudson 2006; Ulloa et al. 2014). Some have obtained the flow field in the cross-junction using numerical simulations (Dylla-Spears et al. 2010).

In none of the studies of cross-slot microchannels, micro-PIV measurements have been carried out simultaneously while a micron-sized object is trapped, and all the researchers relied on the velocity strain field of the flow with the absence of the trapped objects. Simultaneous flow measurements while a target object is trapped (presented in this work) is crucial when relatively large objects are trapped (De Loubens et al. 2015; Gossett et al. 2012), as the average flow strain rate is higher than flow strain rate with the absence of the target, due to obstruction from the target object.

1.3 Present investigation

In our previous work (Akbaridoust et al. 2018), we systematically measured the velocity fields at relatively high strain rate of up to about 140 s^{-1} for different flow rates using micro-PIV and fully characterised the flow to identify the uniform strain rate region. In this work, by modifying the image-based active control technique in cross-slot microchannels we trap single objects in the straining flow (hydrodynamic trap), and simultaneously measure the velocity field using micro-PIV around micron-sized objects while being trapped in the stagnation point. This enables one to calculate the stretching and compressing forces on the filament. It also opens up new vistas of characterising mechanical properties of micron-sized objects. No such measurements have been carried out while a micron-sized object was confined at the stagnation point and all previous studies were based on the measurement of the ideal flow with the absence of the trapped object. Here, we trapped and measured the velocity around filaments of *Anabaena circinalis* [recently renamed *Dolichospermum circinale* by Wacklin et al. (2009)], of the cyanobacteria species, which is a cause of significant water contamination worldwide (Cook et al. 2010). In addition to *A. circinalis*, we grew, trapped and exposed the green alga, *Dunaliella tertiolecta* (the single-celled motile marine species) to demonstrate the capability of the microfluidic trap to confine both motile and non-motile microorganisms and compare the results with the simulation of the microfluidic trap. Although interesting, in this paper, we do not focus on the effects of strain rate on the waterborne microorganisms.

2 Fabrication of microfluidic device

Double-layer microfluidic devices were fabricated with features shown in Fig. 2 using soft lithography. The height and width of the channel are 40 and $400 \mu\text{m}$, respectively (an

aspect ratio of $\alpha_r = h/w = 0.1$). The fabrication protocol of a double-layer microfluidic device (a cross-slot microchannel with an on-chip membrane valve) is thoroughly detailed in Akbaridoust et al. (2016) and Johnson-Chavarria et al. (2014). The black features in Fig. 2 indicate the fluidic channel (cross-slot microchannel) and the red features indicate the control channel (on-chip membrane valve). The protocol suggested by Johnson-Chavarria et al. (2014) was used to manufacture negative photo-lithographic chrome masks for fluidic and control channels using maskless lithography. This step was followed by the fabrication of two master moulds using contact-lithography. The master moulds were comprised of SU-8 cured onto silicon substrates. By casting PDMS against the master moulds, the microchannel features on the moulds were replicated on the PDMS slab. Afterwards, the control channel PDMS replica was peeled off its mould and aligned on the fluidic channel PDMS replica and both were then baked overnight. Finally, the complete PDMS slab was peeled off the mould and plasma-cleaned with oxygen and bonded irreversibly to a cover-slip to form a sealed microfluidic device.

3 Basic concepts of the controlled microfluidic hydrodynamic trap

Functioning of the microfluidic trap is based on the active flow manipulation of the stagnation point to confine objects at the centre of the cross-junction microchannel. Here, a flow-based technique, introduced by Tanyeri et al. (2010), was employed to confine microorganisms at the stagnation point, thereby exposing them to long-term straining flow. This method is an image-based control technique in which the stagnation point is actively repositioned using an on-chip membrane valve to push a target object towards the centre of the cross-slot channel/centre of the trap. In this study, due to the limited resolution of the camera (necessary to decrease the delay time in real-time control) and the shape of the objects, detecting the connections of the filaments of

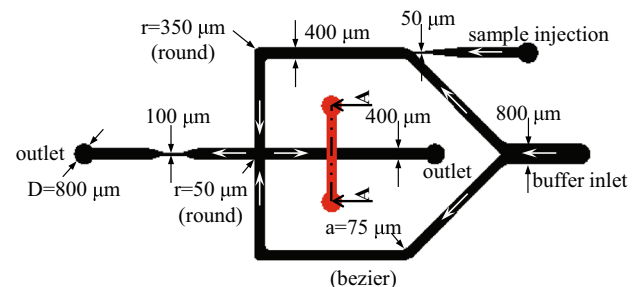


Fig. 2 Cross-slot microchannels fabricated in this work (black: fluidic channel, red: control channel)

A. circinalis (see ESI Sect. 1 for culture growth and maintenance conditions) is challenging. Therefore, a different image-processing method compared to Tanyeri et al. (2010) was used. In Appendix A, we describe the mechanism of the hydrodynamic microfluidic trap including continuous stagnation point repositioning (Appendix A.1), automation of the stagnation point repositioning (Appendix A.2), feedback control algorithm (Appendix A.3) and inline image processing (Appendix A.4).

4 Experimental setup: controlled microfluidic hydrodynamic trap

A programmable syringe pump (Harvard PHD ULTRA) was used to deliver the buffer and sample fluids (e.g. MLA medium containing *A. circinalis*) into the microfluidic device through a 1000 and 250 μL gas-tight glass syringes (Hamilton), respectively. Bent metal tubing (24 gauge, Zephyrtronics) and Luer lock adaptors (Upchurch) were used to establish the connection between the inlets of the microfluidic device and syringes via the PFA tubes (0.020 in ID, 1/16 in OD, IDEX), respectively. A manual micro-shut-off valve (1/16 in OD tubing, Upchurch) was used to block the injection port after a target is trapped in the cross-junction. The same metal tubing and PFA tubes were used to establish the connection between the microfluidic device and the drain reservoir and also to establish the connection between the electronic pressure regulator and the control channel (on-chip membrane valve). The outlet tubes were of equal length and both were submerged into a sample container, thereby maintaining a constant pressure drop in the outlets. An essential oil was used to fill the control channel to avoid permeating the nitrogen to the fluidic channel, which disrupts the water flow and control system.

The microfluidic device was mounted onto an inverted TI-U Eclipse Nikon microscope equipped with a stage-up configuration (two filter block turrets), in which simultaneous imaging with two cameras was possible. This configuration enables streaming the images using a low-resolution and relatively high-frequency camera to control the flow, and simultaneously acquiring high-definition movies using a DSLR camera. For the control, a low-resolution monochrome PointGrey camera (Blackfly 0.3 MP, Gige PoE) capable of streaming images at 90 fps at full resolution was coupled to back port of the microscope using a $0.5\times$ relay lens. For video acquisition, a Nikon D800 camera was used to acquire high-resolution (1080p) colour images at 30 fps.

Images were acquired through a $20\times$ objective lens (CFI S Plan Fluor ELWD). A filter cube holding a 50/50, 45° mirror was placed into one of the microscope turrets to split the light between the two cameras. No extra light source

was used to illuminate the flow for imaging apart from the ambient room lights.

The microfluidic trap is controlled by a custom-built MATLAB code in which inline image processing and online controlling of the devices are carried out (see Appendix A.4 for the inline image processing). The control camera (Pint-Grey) that is directly controlled in the MATLAB environment takes an image of the cross-slot junction when required and streams it to a computer. To control the electronic pressure regulator and the syringe pump, an Arduino UNO controller board was employed (see Appendix A.3 for the feedback control algorithm). The controller is used to send 0–5 V digital signals from MATLAB through its pulse-width modulation (PWM) pins. The signal is amplified to a 0–10 V signal, suitable for the input of the pressure regulator.

To pressurise the control channel, a 2000 psi nitrogen tank was used. Using a manual valve the pressure at the outlet of the tank is reduced to 33 psi, suitable for the inlet of the electronic pressure regulator. A high-resolution electro-pneumatic pressure regulator (Proportion-Air, QPV series) with an accuracy and resolution of $\pm 0.2\%$ and $\pm 0.005\%$, respectively, at full scale was calibrated to provide the outlet pressure at 0–30 psi. This covers the range of the required pressure in the trap simulation explained in ESI Sect. 2. However, the pressure regulator is capable of responding for a pressure change of 1 psi, within 5 and 11 ms when pressurising and relieving the pressure, respectively. This leads to an upper limit of roughly 90 Hz (the same as the camera frequency) for the response time, given that one only needs to change the pressure by 1 psi to keep a particle at the stagnation point. However, according to the simulation of the microfluidic trap (see ESI Sect. 2), after the initial confinement of a target, less than 0.5 psi is sufficient to trap the targets.

4.1 Experimental procedure

In contrast with previous studies that either confined micro-sized objects (e.g. Tanyeri et al. 2010) for long timescales (minutes to hours) and low strain rate (about 1 s^{-1}) or short timescales (De Loubens et al. 2015) (a few milliseconds) and high strain rate (about 500 s^{-1}), here we achieved the confinement of the micron-sized objects at relatively high strain rates (up to 42 s^{-1}) for a relatively long time (up to an hour). This was conducted by programming and synchronising the pump with other equipment and gradually increasing the flow rates using different step functions [see "Appendix A" for the full details of microfluidic operation including feedback control system (Appendix A.3), inline image processing (Appendix A.4) and calibration of the trap (A.5)].

Prior to operating the control system, the syringe pump delivered the fluid through the buffer inlet port at a high flow rate (4000–5000 $\mu\text{L}/\text{h}$) for about 2 min. Delivering the fluid

to the microchannels at high flow rates assists in removing bubbles from the channels. The flow rate was gradually decreased to $50 \mu\text{L/h}$. Prior to injecting the targets, the control system was operated to compute the background (cross-region) and then the shut-off valve was manually opened to inject the targets. Once a target was trapped, the valve was closed manually. After about 1 min of trapping, the flow rate was either kept unchanged or was increased using the functions (cases 1, 2 and 3) shown in Fig. 3. The right-hand side axis of the figure shows the strain rate of each flow rate obtained from micro-PIV experiments in the cross-slot channel with the absence of target objects (Akbaridoust 2017; Akbaridoust et al. 2018). The three functions were defined within the pump in-built interface. The pump was connected to the Arduino controller, thereby sending signals to MATLAB and recording the exact time of triggering the flow rate functions.

5 Simultaneous micro-PIV measurement and real-time control in the hydrodynamics trap

In the microfluidic trap, the necessity of having a relatively large field of view in the control camera (i.e. the whole cross-junction) limits the use of high-magnification microscope objective lenses. Therefore, it is not possible to simultaneously control the flow in the cross-slot channel and measure the velocity field with high resolution near the trapped object's body. Moreover, classical micro-PIV measurement techniques are limited to measuring a two-dimensional velocity field. Hence, apart from the PIV results, we adopt the analytical solution of the flow around an ellipsoidal-shaped object in the straining flow to obtain

the velocity fields. However, it should be noted that one cannot solely rely on the analytical solution of the straining flow over an object, as analytical solution requires the strain rate of the undisturbed flow (away from the trapped object). Although, in previous works, researchers assumed that when the objects are trapped, the strain rate in the flow is the same as the strain rate of the flow with the absence of the target objects, the trapped object may change the flow (De Loubens et al. 2015; Gossett et al. 2012). In the case of trapping of relatively large objects such as *Anabaena circinalis* the average flow strain rate (obtained from the experiments in this work) is higher than flow strain rate with the absence of the target (Akbaridoust 2017; Akbaridoust et al. 2018), due to obstruction from the target object. Hence, using the new micro-PIV measurements we obtain the strain rate with the presence of the target object and substitute it in the analytical solution of the flow over an ellipsoidal object immersed in a creeping straining flow, presented by Jeffery (1922) (see ESI Sect. 3). A combination of the micro-PIV and analytical solution removes the limitation of increasing the resolution of the simultaneous micro-PIV in the controlled straining flow. It should be noted that, one can use 3D particle tracking velocimetry (PTV) using a defocused method (Barnkob et al. 2015; Rossi and Kähler 2014) to avoid using analytical solution. However, the same fundamental optical setup must be used to conduct simultaneous velocity measurement and trapping, and long-term trapping is necessary to acquire enough velocity data points from PTV.

Simultaneous trapping of objects and micro-PIV measurements is challenging because both require their own illumination, optics and camera focused on the micron-sized objects. Employment of a specific wavelength separation enabled us to combine a classical micro-PIV and microfluidic trap setups. The limitations of a simplistic combination of these two setups have been detailed in Appendix B.

5.1 Experiments

All the components in the microfluidic trap experimental setup explained above and a micro-PIV setup (Akbaridoust et al. 2018) were used except for a few minor changes. As can be seen in Fig. 4, a filter cube including the 45° , 50/50 mirror (that splits light to the control camera and PIV camera) and a single-band bandpass filter (420–480 nm, Semrock) was placed into the upper turret of the microscope. While, the epifluorescent cube (G-2A) filter was placed into the bottom turret of the microscope. Figure 5 shows the diagram of the fluorescent intensity of the particles and the transmittance of the filters that are used to simultaneously conduct micro-PIV measurement and real-time control experiment in the microfluidic trap. Using the specifications of these filters, mirrors and particles enable one to conduct simultaneous micro-PIV and trapping. The DSLR camera

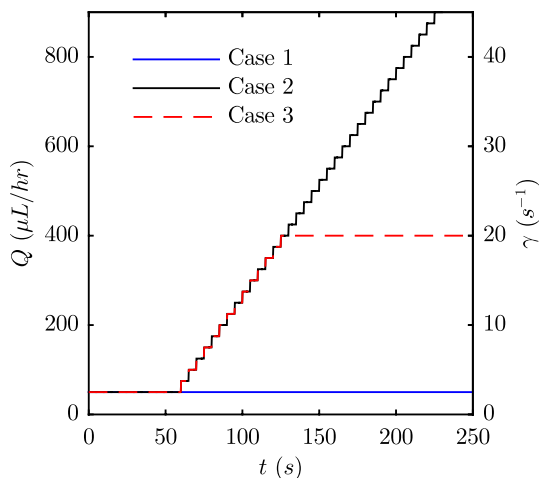


Fig. 3 Flow rate and strain rate variations to be applied in the microfluidic trap after confining a target object

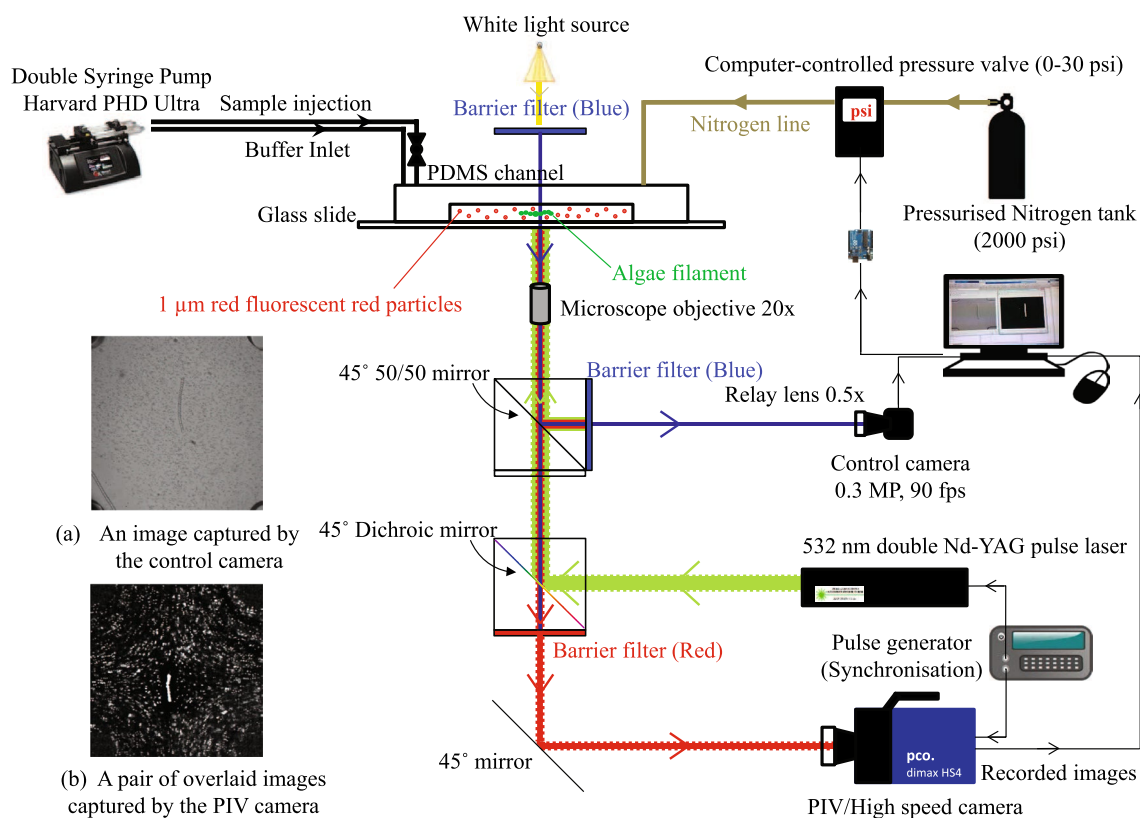


Fig. 4 Schematic of the modified simultaneous micro-PIV and control experimental setups

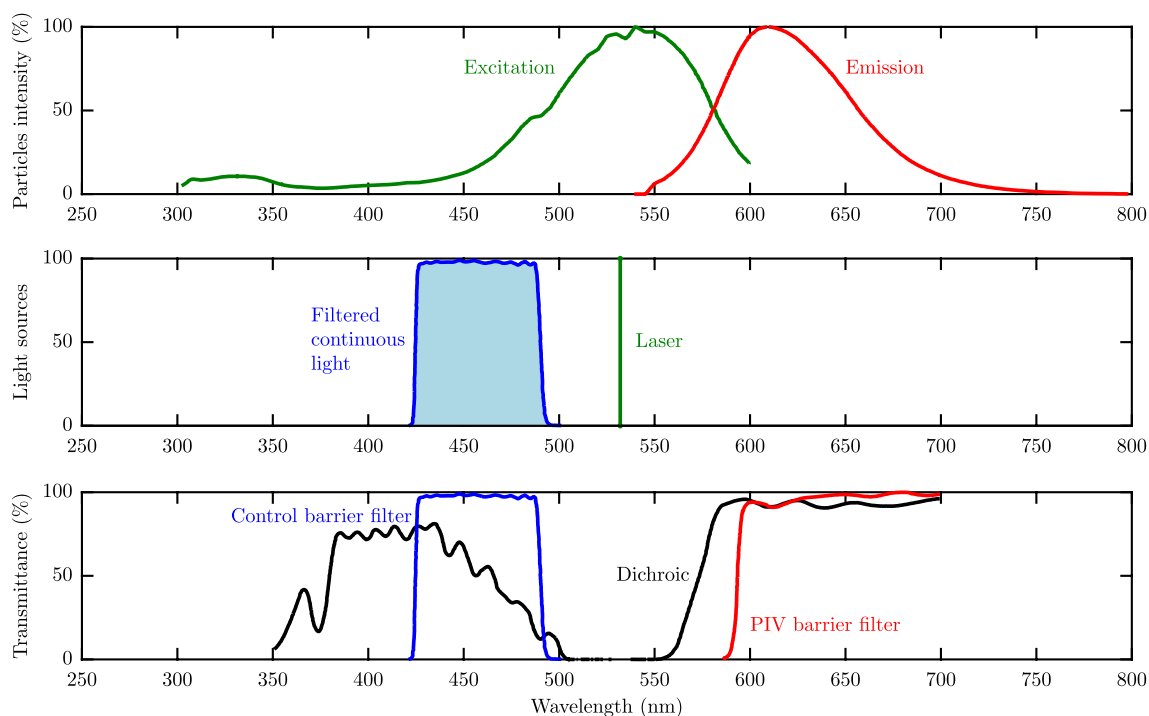


Fig. 5 Excitation and emission of fluorescent-labelled particles and transmittance of barrier, single-band bandpass filters and dichroic mirror (the data were received from Thermo Fisher, Nikon Instruments Co. and Semrock Inc.)

in the hydrodynamic trap experiments was replaced by a high-speed/PIV camera (2000 × 2000 pixels, 12 bits, PCO. dimax HS4), capable of recording images at 2277 fps at full resolution.

As it is impossible to filter the ambient room lights, to filter the light wavelengths of the constant light source, instead of using the ambient room lights, a LumeCube light source (0–1500 Lumens) with the same single-band bandpass filter (420–480 nm, Semrock) used in front of the 50/50 mirror was used to illuminate the flow. Figure 6 shows a photograph of simultaneous micro-PIV and real-time control experimental setup and its components used in this work.

The 1000 μL syringe (connected to the buffer inlets) was filled with water and seeding particles (one micron diameter red fluorescent polystyrene aqueous microspheres, ThermoFisher Scientific), and the 250 μL syringe (connected to the injection port) was filled with the culture medium. To illuminate the seeding particles for micro-PIV, a 532-nm Nd:YAG double-pulsed laser (200 mJ per 9 ns pulse, EverGreen—BigSky Laser Series) that is attenuated and able to double-pulse at 15 Hz was used. The same procedure in trapping was used to run the microfluidic trap and micro-PIV measurements. The pump was operated at a constant rate of 50 $\mu\text{L}/\text{h}$ (case 1 in Fig. 3).

6 Results and discussion

Figure 7 shows three partially overlaid images of the *A. circinalis* strain (ACMR01) that entered the cross-slot region and eventually was trapped in the cross-slot centre (see Movie S1). The trajectory of the filament's centre of

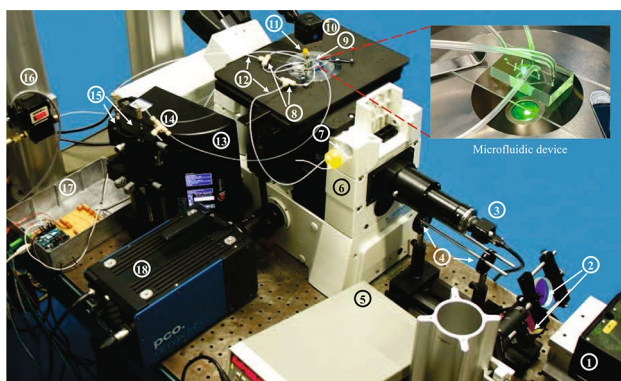


Fig. 6 Photograph of the simultaneous micro-PIV and real-time control experimental setup. 1: Double-pulsed laser, 2: aligning mirrors, 3: control camera, 4: beam expanding lenses, 5: pulse generator, 6: inverted microscope, 7: drained fluid container, 8: T-junction connectors, 9: microfluidic device, 10: LumeCube light source, 11: control channel plug, 12: PFA tubing, 13: double-syringe pump, 14: manual micro-shut-off valve, 15: syringes and connectors, 16: electronic pressure regulator, 17: controller and amplifier, and 18: PIV camera

mass is superimposed on the images and compared with the estimated trajectory of an object in the straining flow without active control [obtained from micro-PIV results in our previous work (Akbaridoust et al. 2018)]. The experimentally measured trajectory of the target is also compared with the simulated trajectory of the target entered at the same position in the same flow rate/strain rate with the same trap centre.

As previously mentioned, with the intention of demonstrating the capability of the microfluidic trap for confinement of both motile and non-motile target objects, we also trapped *D. tertiolecta* species. Figure 8 shows a trapped *D. tertiolecta* cell and its trajectory in the microfluidic device. The experimentally determined trajectory of the *D. tertiolecta* agreed well with the simulation results (shown in Fig. 8), whereas a discrepancy in the experimental results and numerical results can be seen in the case of the trapped *A. circinalis* (shown in Fig. 7). The discrepancy might be rooted in the fact that in the simulation, the target object is simulated by its centroid (a point moving in the straining flow). However, the relatively large size of the *A. circinalis* and its filamentous morphology results in disrupting the hyperbolic streamlines of the flow, whereas the *Dunaliella*, which is much smaller than *A. circinalis* and spherical in shape, follows the flow streamlines with less influence on them. Therefore, there was less discrepancy between the simulation and the experimental results.

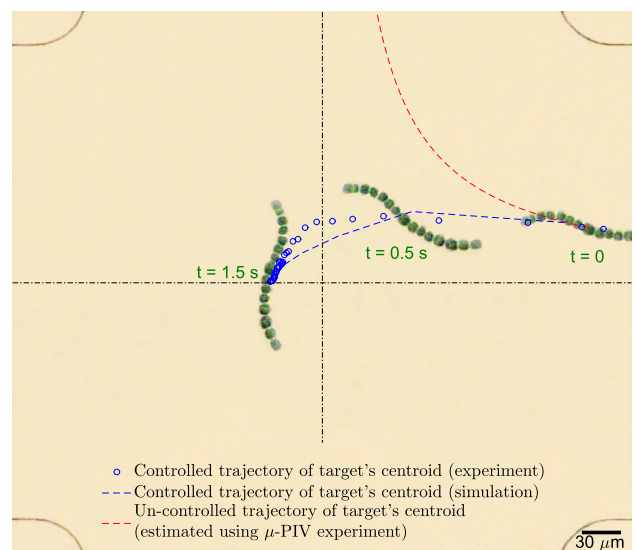


Fig. 7 Three partially overlaid images of the confinement of the *A. circinalis* filament (ACMR01) in the cross-slot junction using active control system at $Q = 50 \mu\text{L}/\text{h}$ and $\gamma = 2.3 \text{ s}^{-1}$ (see Movie S1). The experimentally measured target's trajectory is shown by blue circles, whereas the blue dash line shows the numerically estimated target's trajectory. The red dash line shows the streamline of the flow with the absence of the control system (obtained from micro-PIV experiments)

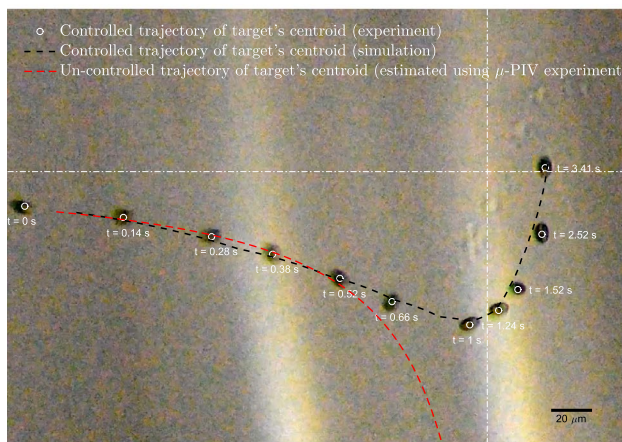


Fig. 8 Eleven partially overlaid images of the confinement of a *Dunaliella tertiolecta* in the cross-slot junction using an active control system at $Q = 100 \mu\text{L/h}$. The experimentally measured target's trajectory is shown by white circles, whereas the black dash line shows the numerically estimated target trajectory. The red dash line shows the streamline of the flow with the absence of the control system

6.1 Simultaneous micro-PIV results

Using the simultaneous micro-PIV and trapping method in the cross-slot microchannels, the velocity field around the trapped filaments was measured. Figure 9 shows an example of six overlaid image pairs captured by the PIV camera sensor while a filament of *A. circinalis* was trapped in the cross-junction (see Movie S2). For the purpose of displaying the image, the image was post-processed and converted to a black and white image. Therefore, the particles appear slightly larger than the real size captured by the camera sensor. Apart from the red tracer particles, images of the blue-green *A. circinalis* filament were recorded by the PIV camera sensor, in spite of the presence of the barrier filter (that blocks all the wavelengths except red) with the specifications shown in Fig. 5. This is due to the existence of the chlorophyll in the *A. circinalis* filament. Although chlorophyll appears green when it absorbs white light, regardless of the light source, it emits red wavelength as well (Hall et al. 1993). In the figure it is noted that the filament is surrounded by a no-particle/-flow region (shown with the red dash line in Fig. 9) indicating the presence of mucilage around the filament. Cyanobacteria produce mucilaginous sheaths to protect themselves from other deleterious microorganisms (Amsler 2008; Pajdak-Stós et al. 2001). As the mucilage was not washed off from the filament while exposed to the straining flow, we consider both the filament and the sheath a single solid object.

The same pre-processing, processing and post-processing techniques used in our previous work (Akbaridoust 2017;

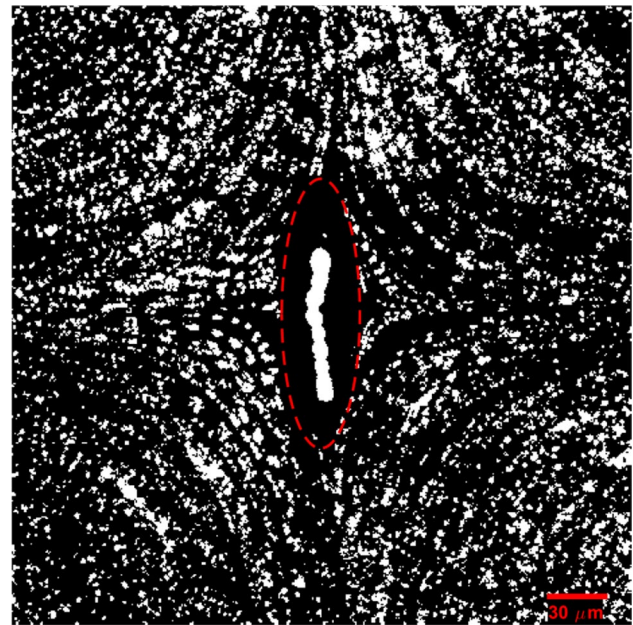


Fig. 9 An example of six overlaid image pairs while a filament of *A. circinalis* was trapped in the cross-junction (see Movie S2)

Akbaridoust et al. 2018) were implemented to calculate the velocity field in the cross-slot junction of the microchannel.

To find the strain rate (γ), which is required to be substituted in the analytical solution (see ESI Sect. 2.2), the gradients of the velocity field away from the trapped object is calculated using a least square fitting method used in our previous work (Akbaridoust et al. 2018). The calculated strain rate was $\gamma = 3.2 \text{ s}^{-1}$ at $Q = 50 \mu\text{L/h}$, whereas $\gamma = 2.3 \text{ s}^{-1}$ at the same flow rate with the absence of the trapped filament (Akbaridoust et al. 2018) results in a change of about 40%. By substituting this value into the analytical solution, the velocity fields obtained from micro-PIV and analytical solution are compared in Fig. 10. The black vectors in Fig. 10 are the ensemble-average velocity vector map in the cross-junction around the trapped filament shown in Fig. 9, while the red vectors that match closely with the micro-PIV results show the analytical solution by Jeffery (1922).

To more clearly show the agreement between the PIV results and analytical solution, the u -component velocity profile at $y = 0$ (along the compressional axis) is plotted in Fig. 11 and also compared with the velocity profile when the flow was not disturbed by the trapped filament. As can be seen, the gradient of the measured velocity field is higher by about 40% than that of the velocity with the absence of the trapped filament ($u = \gamma x$). This is due to the cross-region being occupied by the trapped target, which in turn reduces the cross-slot area, increases the flow speed and hence the strain rate.

In addition to the strain rate of the flow far from the object with about 40% deviation, the strain rate in the

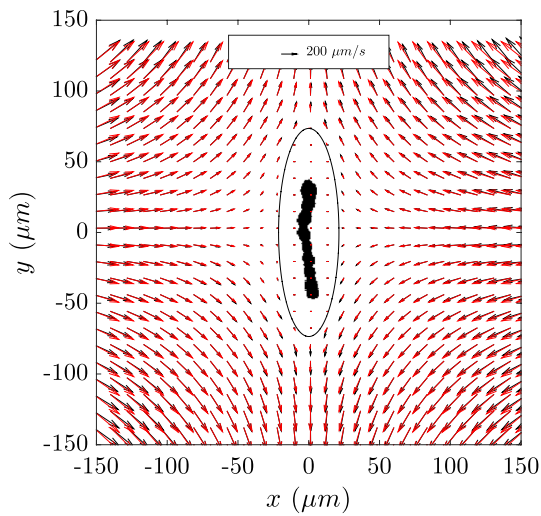


Fig. 10 Comparison of the ensemble-average velocity vectors (black vectors) obtained from micro-PIV measurement around a filament of the *A. circinalis* (shown in Fig. 9) and the velocity vectors (red vectors) analytically obtained from Jeffery (1922) around an ellipsoid

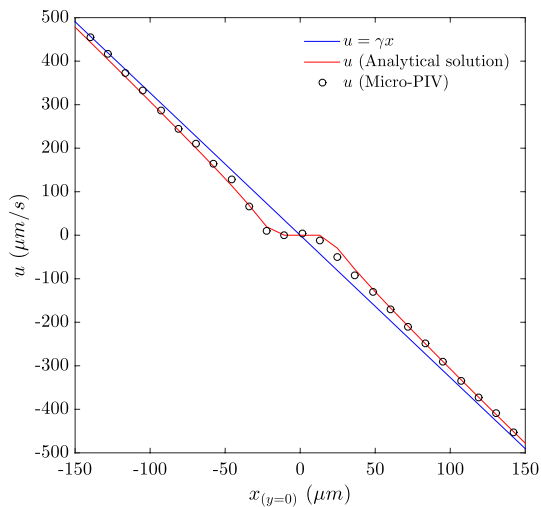
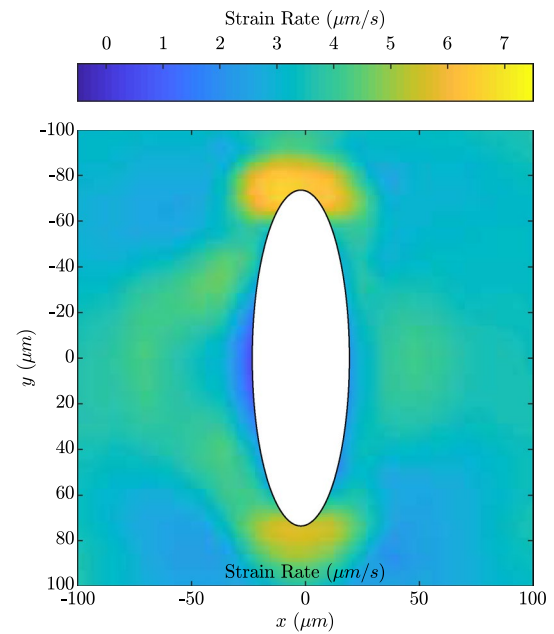
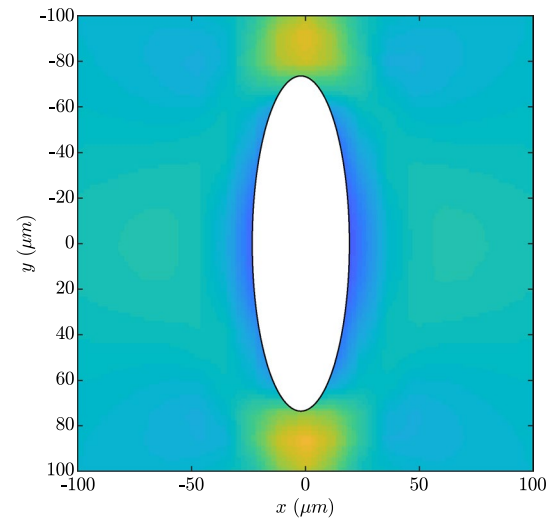


Fig. 11 Comparison of the u -component velocity profile at $y=0$ (along the compressional axis) obtained from micro-PIV measurements and analytical solution (Jeffery 1922) and pure straining flow

whole cross-slot region was deviated from the pure straining flow. Figure 12 shows the contour of the strain rate around the object calculated from micro-PIV measurements (Fig. 12a) and analytical solution (Fig. 12b). The slight asymmetric contour map in Fig. 12a is due to the asymmetric shape of the filament and the sheath that it is encapsulated with. The strain rate contour reveals that the ellipsoidal object experienced a higher extensional force than compressional force, where the strain rate in the extensional region is about three times higher than that



(a) micro-PIV



(b) Analytical solution

Fig. 12 Spatial variation of the strain rate in the cross-slot region around the trapped target

of the pure straining flow and in the compressional region is half of strain rate in pure straining flow.

In our experiments, we observe neither mechanical damage to, nor any dramatic deformation in, the filaments of cyanobacteria. Therefore, at present, it is challenging to obtain the mechanical properties of the cyanobacteria from the experiments. However, one can calculate the mechanical properties of an ellipsoidal object using the present experimental setup and measurement techniques if the object is deformed.

7 Summary and conclusions

In this paper, we reported the use of a fully quantified stagnation point flow in a cross-slot-type microfluidic device equipped with an image-based real-time control system and simultaneously quantified by micro-PIV measurements.

In the first set of experiments, the microorganisms were confined in the cross-slot-type microfluidic device using the image-based active control system. Using a specific combination of image-processing techniques resulted in accurate detection and confinement of the filaments of *A. circinalis*. Due to the small size of the cell connections in *A. circinalis* filaments and using a camera with a low resolution (necessary to operate the active control system at a high speed), the cell connections were not detectable by the control camera. Using a morphologically close image-processing operation by a rectangular-shaped structural element, we increased the connectivity of the blobs without distorting them, thereby computing the correct position of the centroid of the target.

A large number of round motile (*Dunaliella tertiolecta*) and filamentous (*A. circinalis*) non-motile microorganisms were successfully trapped for up to an hour at the stagnation point of the controlled straining flow. Prior to the experiments we predicted the trajectory of the target object in the controlled flow. The experimentally determined trajectory of the *D. tertiolecta* agreed well with the simulation results, whereas for *A. circinalis* a discrepancy in the experimental results and numerical results was observed. The discrepancy is likely due to the fact that in the simulation, the target object is simulated by its centroid (a point moving in the straining flow). However, the relatively large size of the *A. circinalis* and its filamentous morphology results in disrupting the hyperbolic streamlines of the flow, whereas the *D. tertiolecta*, which is much smaller than *A. circinalis* and spherical in shape, follows the flow streamlines with less influence on them.

In contrast with previous studies that either confined micro-sized objects for long timescales (minutes to hours) and low strain rate (about 1 s^{-1}) (Johnson-Chavarria et al. 2011, 2014; Latinwo et al. 2014; Li et al. 2015; Shenoy et al. 2015; Tanyeri and Schroeder; Tanyeri et al. 2010, 2011) or short timescales (a few milliseconds) and high strain rate (about 500 s^{-1}) (Cha et al. 2012; Gossett et al. 2012; Henon et al. 2014; Henry et al. 2013), we achieved the confinement of the micron-sized objects at relatively high strain rates (up to 42 s^{-1}) for a relatively long time (up to an hour). This was conducted by programming and synchronising the pump with other equipment and gradually increasing the flow rates using different step functions. This enables one to use this platform to study the effect of high and long-term straining flow on single micron-sized objects.

In a second set of the experiments, micro-PIV measurements and real-time control were simultaneously carried out to measure the velocity field around a trapped target. Two major problems were encountered by combining the two experimental setups (micro-PIV setup and microfluidic trap setup). The first issue was the disruption of the control camera by the laser pulses that prevents the detection of a target object in the micro-cross channel. The second issue was the production of extremely bright background in the images acquired by the PIV camera sensor due to the constant white light source, which precludes correlating the recorded images.

We successfully implemented a modification to the experimental setup to address the two issues explained above. To tackle the first issue, we replaced the continuous white light with a continuous blue light source (i.e. filtering all the wavelengths except blue). Whilst, to address the second issue, we filtered all the wavelengths (except blue) incident on the control camera sensor. Using this arrangement, the control camera sensor does not capture the laser pulses, and the PIV camera does not acquire the bright background caused by the constant light source.

Carrying out these experiments and combining the experimental results with an analytical solution of flow around an ellipsoidal object immersed in a straining flow (Jeffery 1922) enable one to accurately obtain the velocity near the trapped target, regardless of the micro-PIV resolution.

In the case of trapping relatively large objects such as *A. circinalis*, the average flow strain rate (obtained from the experiments) was higher than flow strain rate with the absence of the target, due to obstruction from the target object. The increase in the strain rate was about 40%. However, this depends on the size of the object compared to the dimensions of the cross-slot junction.

Electronic Supplementary Information (ESI) available: We provide the culture growth and maintenance conditions (ESI Sect. 1); simulation of the control system to trap a target object (Sect. 2); analytical solution of the flow over an ellipsoidal object immersed in a creeping straining flow (Sect. 3); videos of trapping a single filament of *A. circinalis* (movie S1), and particles flowing around a single filament (movie S2) are also provided.

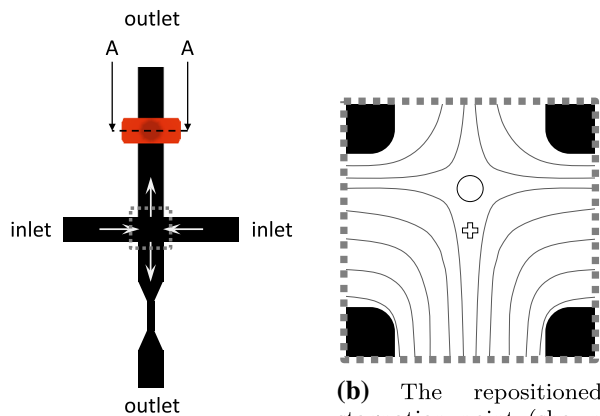
Acknowledgements The authors gratefully acknowledge the Australian Research Council for the financial support of this work. This work was performed in part at the Melbourne Centre for Nanofabrication (MCN) in the Victorian Node of the Australian National Fabrication Facility (ANFF).

Appendix A: Mechanism of the microfluidic hydrodynamic trap

A.1: Continuous stagnation point repositioning

If the two outlets of the cross channel have the same flow resistance, the inlet streams are equally bifurcated to the two outlets. If there is a constraint on one of the outlets (e.g. the constraint shown at the bottom outlet in Fig. 13a), the outlet flow rates will no longer be the same because of the inequality in the flow resistance of the outlets. Moreover, the stagnation point is displaced towards the outlet with higher flow resistance. Therefore, if the cross-sectional area of the outlets constantly varies, the stagnation point will be continuously repositioned along the extensional axis.

In this work, repositioning the stagnation point (shown in Fig. 13b) is conducted by implementing a fixed width constriction in one of the outlets, and a variable height constriction on the other (Tanyeri et al. 2010). The former is shown in the bottom outlet and the latter is shown in red on the top outlet in Fig. 13a. Figure 13c shows the section A–A of the variable height constriction, known as an on-chip membrane valve (in Fig. 13a), and how its deformation constricts the height of the fluidic channel. The control channel is filled with pressurised gas, which results in the deflection of the thin membrane, thereby constricting the height of the fluidic channel. It is called the variable constriction because changes in the gas pressure leads to changes in the deflection of the membrane, and consequently constrict the channel at different heights.

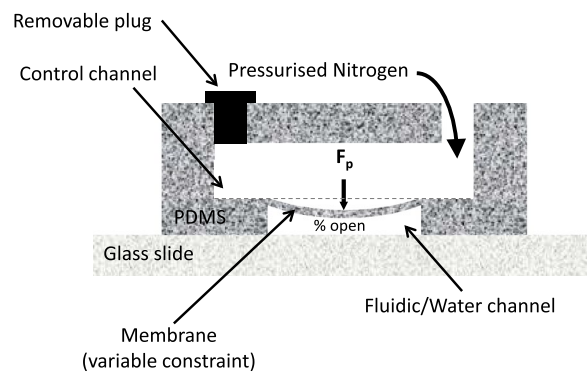


(a) The cross-slot junction with a fixed width constriction (bottom outlet) and a variable height constriction (the red feature on the top outlet).

(b) The repositioned stagnation point (shown with a circle), moved towards the top outlet in figure 13a.

A.2: Automation of the stagnation point repositioning to confine a target object at the channel centre

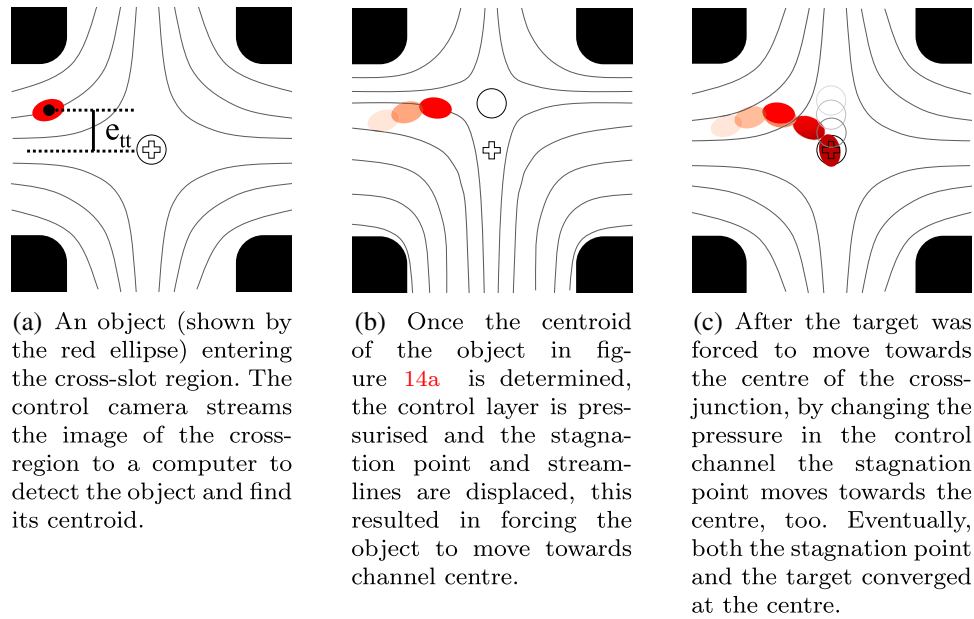
In the microfluidic hydrodynamic trap, when a target object enters the cross-slot region (shown in Fig. 14a), a camera captures and streams the image of the cross-junction to a computer. Using image-processing methods the shape of the object is determined and the position of the object centroid is computed. Based on the location of the object in extensional direction, the ratio of the outlet flow rates is changed and consequently the stagnation point is repositioned. The repositioning is carried out using the on-chip membrane valve, which allows the flow streamlines to be manipulated. This manipulation places the target object between the stagnation point and the centre of the channel (shown in Fig. 14b), thereby exerting a hydrodynamic force on the target object towards the trap centre. The manipulation results in placing the object on a new streamline and moving the object towards the channel centre. All of these steps are repeated until both the target and the stagnation point converge in the centre of the trap/channel (shown in Fig. 14c), and at this stage the pressure stays unchanged. However, if due to an external or internal disturbance the target object is displaced from the centre, the same procedure is re-applied forcing the object to return to the centre.



(c) The side A–A section of the channel in figure 13a and the deflected membrane valve that constrained the height of the channel.

Fig. 13 Different views of the cross-slot junction with the two fixed and variable constraints on the outlets and the effect of the constraint on the stagnation point position and streamlines

Fig. 14 The effect of displacing the stagnation point on the flow streamlines and the trajectory of an object in cross-junction. The red ellipse, solid black circle, hollow circle and the hollow cross represent the target object, its centroid, the stagnation point and the centre of the channel, respectively



A.3: Feedback control algorithm

A linear feedback control algorithm was implemented to update the pressure in the control layer and displace the stagnation point using (Tanyeri et al. 2010):

$$P_{\text{val}} = P_{\text{tc}} + K_p K_C e_{\text{tt}}, \quad (1)$$

where P_{val} is the pressure in the control channel (on-chip valve), P_{tc} is the required pressure to keep the stagnation point at the trap centre. The proportional gain is presented by K_p and it can be considered as a constant ($K_p = -1.5$) and K_C is a factor to convert pressure to distance. If there is a linear relation between the pressure and the stagnation point position, K_C will be a constant. The offset error (e_{tt}) in Eq. 1 is defined as

$$e_{\text{tt}} = Y_{\text{tp}} - Y_{\text{tc}}, \quad (2)$$

which is the distance between the position of target (Y_{tp}) and trap centre (Y_{tc}) along the extensional axis (shown in Fig. 14a). Figure 15 depicts the flowchart of the steps employed for confining a target object in the centre of the cross-slot junction.

A.4: Inline image processing

In this work, the foreground detection was carried out using the “Computer Vision System” toolbox in MATLAB. This includes acquiring the cross-region as the background and comparing it with the image of the target in the cross-region. Image comparison was followed by determining whether each pixel belongs to the background (channel) or the foreground (target). Before and after the foreground detection,

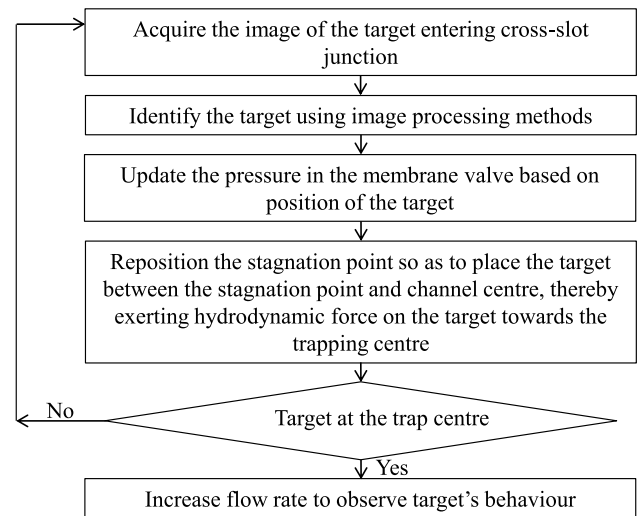


Fig. 15 Algorithm for confining a target object in the cross-slot region of the microchannel, which is schematically shown in Fig. 14

image contrast enhancement and some morphological operations were carried out to improve in locating the accuracy the target's centroid.

Figure 16 depicts the implementation of the image-processing steps used in the present work to locate the centroid of the *A. circinalis* filament. First, the background image of the region of interest (ROI) was acquired. This was conducted prior to the filament entering ROI (partially shown in Fig. 16a). Figure 16b shows a filament of the cyanobacteria in the ROI. Upon acquiring the image of the target (filament), the image contrast was enhanced to increase pixel intensity of the filament (shown in Fig. 16c). Afterwards, the foreground was detected. Foreground detection requires

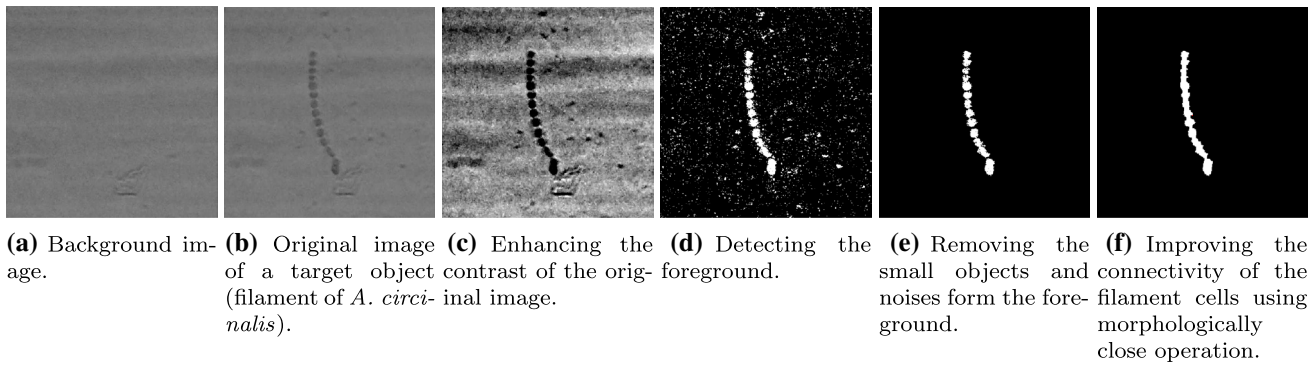


Fig. 16 Implementation of the image-processing steps that were used for foreground detection (detecting the *A. circinalis* filament in the micro-channel)

defining a threshold parameter that depends on the light condition to determine whether each pixel belongs to the channel or the target. The background was then subtracted from the foreground, thereby achieving the target object mask (the binary image shown in Fig. 16d). This step was followed by removing small objects and noises, by defining a certain threshold and removing the blobs (connected white regions) smaller than the threshold (shown in Fig. 16e). Due to the low resolution of camera and the shape of the objects, detecting the connections of the filaments is challenging. As can be seen, the connections are neither observable in Fig. 16b, nor detectable in Fig. 16e. To alleviate this issue, we used morphologically close operation by a 7×7 -pixel square-shaped structural element to increase the connectivity of the blobs without over-fattening it. Stated in Smith et al. (1997), morphologically close operation in processing of a binary image includes a morphologically erosive operation (making the blob smaller) followed by a morphologically dilative operation (making the blob larger). Figure 16f shows the post-processed mask of the filament after applying the morphologically close operation. Eventually, the centroid of the filament was determined using the blob analysis of the MATLAB computer vision system toolbox.

A.5: Calibrating the microfluidic trap

The calibration curve of the microfluidic trap is the variation of the stagnation point position at different control channel pressures. The linear region of this curve is used to determine the conversion factor (K_C in Eq. 1). To experimentally determine this curve, a fluid visualisation experiment was conducted, which delivered the fluid seeded with tracer particles to the cross-junction. By capturing the images of the cross-region, the flow is visualised. In this experiment, the flow was illuminated using the Nikon microscope Epi-fl illuminator (Mercury lamp). The epifluorescence imaging setup configuration that was used in micro-PIV experiments Akbaridoust et al. (2018), except the PIV camera that was

replaced by the control camera was employed to acquire the images. The backgrounds (out-of-focus particles) of the acquired images were then removed Akbaridoust et al. (2018) and then 150 images were overlaid. This procedure was repeated at the different pressures in the control channel, and for each set of images the stagnation point was determined manually/visually with the accuracy of one pixel. One pixel corresponds to one micron for the control camera used in this experiment.

Figure 17 shows an example of 150 overlaid images at the flow rate of $50 \mu\text{L/h}$ and control channel pressure of about 8 psi. The distance of the stagnation point position from the centre line of the channel along the extensional and compressional axes are represented by Y_o and X_o , respectively. As can be seen, the stagnation point is not located on the vertical centre line, due to the flow added to one of the inlets where the sample injection port is located. However, $X_o \neq 0$ only occurs when the injection port is open. In trapping

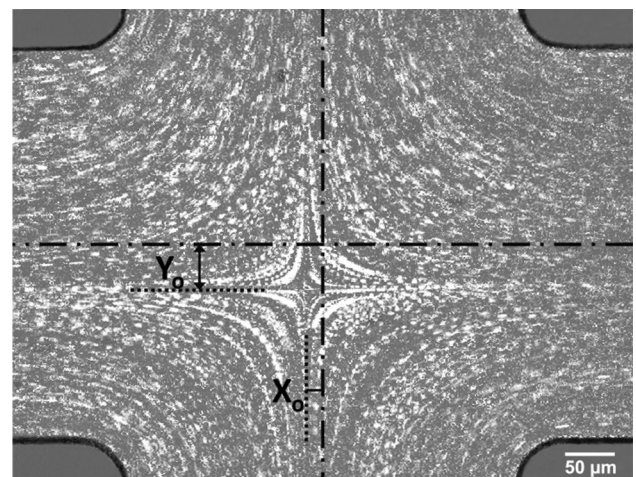


Fig. 17 An example image of 150 overlaid recordings (at the flow rate of $50 \mu\text{L/h}$ and control channel pressure of about 8 psi) that were used to determine the calibration curve of the microfluidic trap

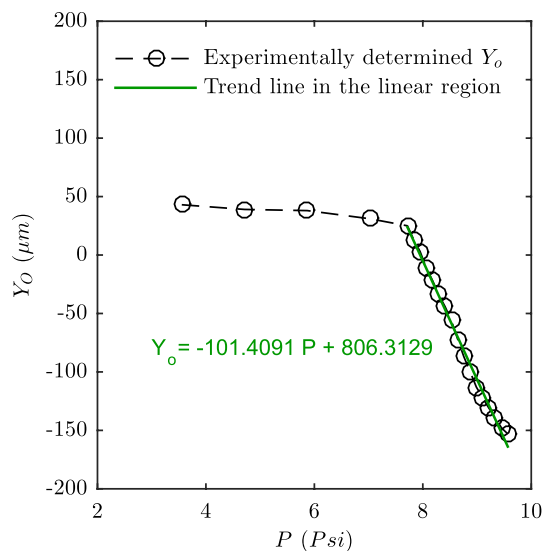


Fig. 18 Experimentally determined calibration curve of the microfluidic trap. The green line is the trend line fitted to the linear region, and the slope of this line represents the conversion factor (K_C)

experiments once a target is trapped, the injection port is manually closed and the stagnation point gradually moves on the centre line along the compressional axis. Figure 18

shows the calibration curve that was experimentally determined (at 50 $\mu\text{L/h}$) at different pressures in the control channel. The slope of the fitted trend line represents the conversion factor (K_C).

Appendix B: Methodology of simultaneous micro-PIV measurements and trapping

In principle, the use of volume illumination in PIV measurements results in bright background in the images that drastically reduce the signal-to-noise ratio and the correlation peak detectability. Therefore, in micro-PIV, the epifluorescence imaging technique (i.e. illuminating the fluorescent particles by green pulsed light and capturing the red light from them) is implemented to alleviate this issue (Santiago et al. 1998). In hydrodynamic microfluidic trap experiments (in this work and also Schroeder and co-workers (Johnson-Chavarria et al. 2011, 2014; Latinwo et al. 2014; Li et al. 2015; Shenoy et al. 2015; Tanyeri and Schroeder; Tanyeri et al. 2010, 2011), a constant white light source (here ambient room lights) was used for imaging. Hence, simultaneous trapping of objects and micro-PIV measurements is challenging because both require their own illumination, optics

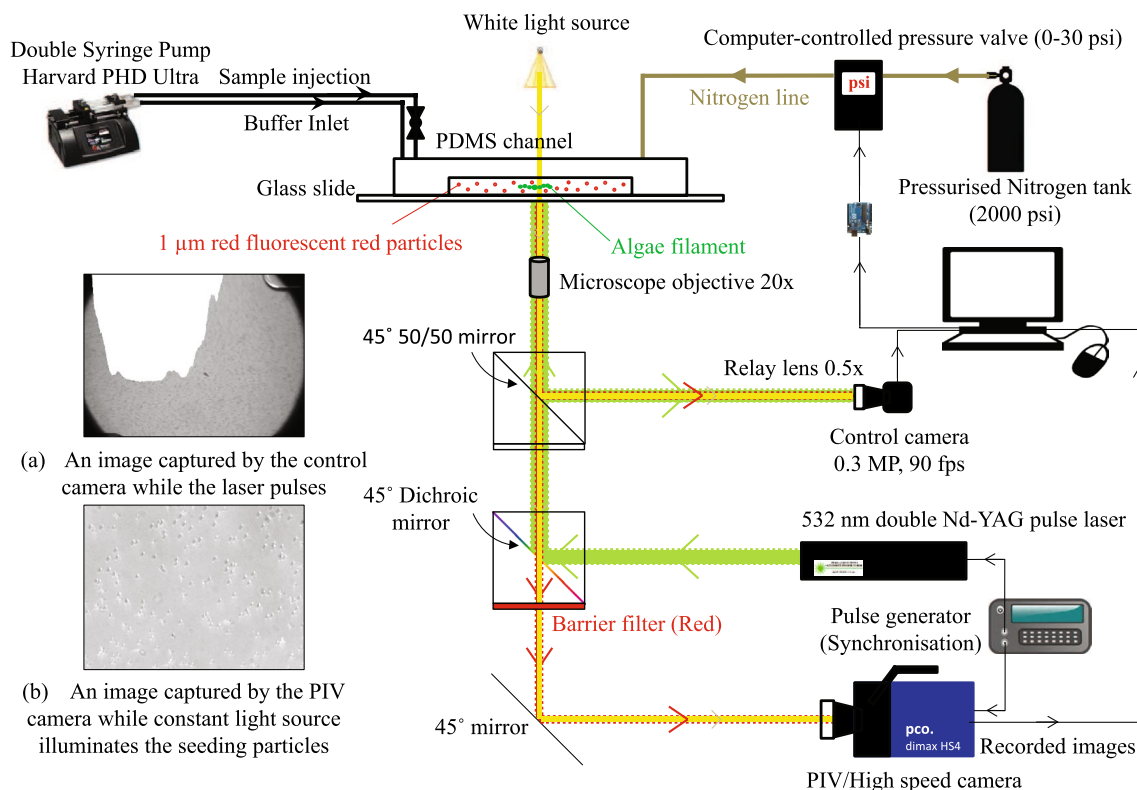


Fig. 19 Schematic of the combination of micro-PIV and active control setups and the resulting imaging problems in the images acquired by the PIV and the control camera

and camera focused on the micron-sized objects. Simply combining the two experimental setups (micro-PIV and the microfluidic trap setups) to conduct simultaneous micro-PIV measurements and trapping in the microfluidic device leads to two major problems. The combination of the two setups is shown in Fig. 19. The first issue is the disruption of the control camera by the laser pulses. The second issue is the production of an extremely bright background in the images acquired by the PIV camera sensor due to the constant white light source. The former results in preventing the detection of a target object in the cross-slot channel. The top inset image in Fig. 19a shows an example of the image captured by the control camera when the laser was pulsing. As can be seen, the laser pulse interferes with the image-processing techniques for object detection. While, the latter is the production of extremely bright background that precludes correlating the recorded images. The bottom inset image in Fig. 19b shows an image of the particles captured by the PIV camera, while the constant white light was illuminating the flow.

To tackle the first issue we replaced the continuous white light with a continuous blue light source (i.e. filtering all the wavelengths except blue). Whilst, to address the second issue, we filtered all the wavelengths (except blue) incident on the control camera sensor. Using this arrangement, the control camera sensor does not capture the laser pulses, and the PIV camera does not acquire the bright background caused by the constant light source. Figure 4 shows the schematic of the combined micro-PIV and active control system setups, where the two problems that were pointed out are solved using two single-band (blue) bandpass filters. The bandpass filters block all the wavelengths out of the range 420–480 nm.

References

- Akbaridoust F (2017) Characterisation of a microfluidic hydro-trap to study the effect of straining flow on waterborne microorganisms. Ph.D. thesis, University of Melbourne
- Akbaridoust F, Philip J, Marusic I (2016) A miniature high strain rate device. In: Proceedings of 20th AFMC conference
- Akbaridoust F, Philip J, Marusic I (2018) Assessment of a miniature four-roll mill and a cross-slot microchannel for high-strain-rate stagnation point flows. *Meas Sci Technol* 29(4):045302
- Alicia TGG, Yang C, Wang Z, Nguyen N-T (2016) Combinational concentration gradient confinement through stagnation flow. *Lab Chip* 16(2):368–376
- Amsler CD (2008) *Algal chemical ecology*, vol 468. Springer, Berlin
- Ashkin A, Dziedzic JM, Bjorkholm JE, Chu S (1986) Observation of a single-beam gradient force optical trap for dielectric particles. *Opt Lett* 11(5):288–290
- Barnkob R, Kähler CJ, Rossi M (2015) General defocusing particle tracking. *Lab Chip* 15(17):3556–3560
- Bernassau AL, Glynne-Jones P, Gesellchen F, Riehle M, Hill M, Cumming DRS (2014) Controlling acoustic streaming in an ultrasonic heptagonal tweezers with application to cell manipulation. *Ultrasonics* 54(1):268–274
- Cha S, Shin T, Lee SS, Shim W, Lee G, Lee SJ, Kim Y, Kim JM (2012) Cell stretching measurement utilizing viscoelastic particle focusing. *Anal Chem* 84(23):10471–10477
- Cook PLM, Holland DP, Longmore AR (2010) Effect of a flood event on the dynamics of phytoplankton and biogeochemistry in a large temperate Australian lagoon. *Limnol Oceanogr* 55(3):1123–1133
- Curtis MD, Sheard GJ, Fouras A (2011) Feedback control system simulator for the control of biological cells in microfluidic cross slots and integrated microfluidic systems. *Lab Chip* 11(14):2343–2351
- De Loubens C, Deschamps J, Boedec G, Leonetti M (2015) Stretching of capsules in an elongation flow, a route to constitutive law. *J Fluid Mech* 767:R3
- Dylla-Spears R, Townsend JE, Jen-Jacobson L, Sohn LL, Muller SJ (2010) Single-molecule sequence detection via microfluidic planar extensional flow at a stagnation point. *Lab Chip* 10(12):1543–1549
- Gosse C, Croquette V (2002) Magnetic tweezers: micromanipulation and force measurement at the molecular level. *Biophys J* 82(6):3314–3329
- Gossett DR, Henry TK, Lee SA, Ying Y, Lindgren Anne G, Yang OO, Rao J, Clark AT, Di Carlo D (2012) Hydrodynamic stretching of single cells for large population mechanical phenotyping. *PNAS* 109(20):7630–7635
- Grier DG (2003) A revolution in optical manipulation. *Nature* 424(6950):810–816
- Hall DO, Scurlock JMO, Bolhar-Nordenkampf HR, Leegood RC, Long SP (1993) *Photosynthesis and production in a changing environment: a field and laboratory manual*. Chapman & Hall, London
- Henon Y, Sheard GJ, Fouras A (2014) Erythrocyte deformation in a microfluidic cross-slot channel. *RSC Adv* 4(68):36079–36088
- Henry TK, Gossett DR, Moon YS, Masaeli M, Sohsman M, Ying Y, Mislick K, Adams RP, Rao J, Carlo DD (2013) Quantitative diagnosis of malignant pleural effusions by single-cell mechanophenotyping. *Sci Transl Med* 5(212):212ra163–212ra163
- Hertz HM (1995) Standing-wave acoustic trap for nonintrusive positioning of microparticles. *J Appl Phys* 78(8):4845–4849
- Jeffery GB (1922) The motion of ellipsoidal particles immersed in a viscous fluid. *Proc R Soc Lond A* 102(715):161–179
- Johnson-Chavarria EM, Tanyeri M, Schroeder CM (2011) A microfluidic-based hydrodynamic trap for single particles. *J Vis Exp* 47:e2517–e2517
- Johnson-Chavarria EM, Agrawal U, Tanyeri M, Kuhlman TE, Schroeder CM (2014) Automated single cell microbioreactor for monitoring intracellular dynamics and cell growth in free solution. *Lab Chip* 14(15):2688–2697
- Latinwo F, Hsiao K-W, Schroeder CM (2014) Nonequilibrium thermodynamics of dilute polymer solutions in flow. *J Chem Phys* 141(17):174903
- Lee H, Purdon AM, Westervelt RM (2004) Manipulation of biological cells using a microelectromagnet matrix. *Appl Phys Lett* 85(6):1063–1065
- Li Y, Hsiao K-W, Brockman CA, Yates DY, Robertson-Anderson RM, Kornfield JA, San Francisco MJ, Schroeder CM, McKenna GB (2015) When ends meet: circular DNA stretches differently in elongational flows. *Macromolecules* 48(16):5997–6001
- Pajdak-Stós A, Fiakowska E, Fyda J (2001) *Phormidium autumnale* (cyanobacteria) defense against three ciliate grazer species. *Aquat Microb Ecol* 23(3):237–244
- Pathak JA, Hudson SD (2006) Rheo-optics of equilibrium polymer solutions: wormlike micelles in elongational flow in a microfluidic cross-slot. *Macromolecules* 39(25):8782–8792
- Perkins TT, Smith DE, Chu S (1997) Single polymer dynamics in an elongational flow. *Science* 276(5321):2016–2021

- Qiu Y, Wang H, Demore CEM, Hughes DA, Glynne-Jones P, Gebhardt S, Bolhovitins A, Poltarjonoks R, Weijer K, Schönecker A et al (2014) Acoustic devices for particle and cell manipulation and sensing. *Sensors* 14(8):14806–14838
- Rossi M, Kähler CJ (2014) Optimization of astigmatic particle tracking velocimeters. *Exp Fluids* 55(9):1809
- Santiago JG, Wereley ST, Meinhart CD, Beebe DJ, Adrian RJ (1998) A particle image velocimetry system for microfluidics. *Exp Fluids* 25(4):316–319
- Schroeder CM, Babcock HP, Shaqfeh ESG, Chu S (2003) Observation of polymer conformation hysteresis in extensional flow. *Science* 301(5639):1515–1519
- Schroeder CM, Shaqfeh ESG, Chu S (2004) Effect of hydrodynamic interactions on DNA dynamics in extensional flow: simulation and single molecule experiment. *Macromolecules* 37(24):9242–9256
- Shenoy A, Tanyeri M, Schroeder CM (2015) Characterizing the performance of the hydrodynamic trap using a control-based approach. *Microfluid Nanofluid* 18(5–6):1055–1066
- Shenoy A, Rao CV, Schroeder CM (2016) Stokes trap for multiplexed particle manipulation and assembly using fluidics. *PNAS* 113(15):3976–3981
- Smith SW et al (1997) The scientist and engineer's guide to digital signal processing. California Technical Publications, San Diego
- Tanyeri M, Schroeder CM (2013) Manipulation and confinement of single particles using fluid flow. *Nano Lett* 13(6):2357–2346
- Tanyeri M, Johnson-Chavarria EM, Schroeder CM (2010) Hydrodynamic trap for single particles and cells. *Appl Phys Lett* 96(22):224101
- Tanyeri M, Ranka M, Sittipolkul N, Schroeder CM (2011) A microfluidic-based hydrodynamic trap: design and implementation. *Lab Chip* 11(10):1786–1794
- Taylor GI (1934) The formation of emulsions in definable fields of flow. *Proc R Soc Lond A* 146(858):501–523
- Ulloa C, Ahumada A, Cordero M (2014) Effect of confinement on the deformation of microfluidic drops. *Phys Rev E* 89(3):033004
- Wacklin P, Hoffmann L, Komárek J et al (2009) Nomenclatural validation of the genetically revised cyanobacterial genus. *Dolichospermum* (Ralfs ex Bornet et Flahault) comb. nova. *Fottea* 9(1):59–64
- Weilin X, Muller SJ (2011) Exploring both sequence detection and restriction endonuclease cleavage kinetics by recognition site via single-molecule microfluidic trapping. *Lab Chip* 11(3):435–442
- Yang AHJ, Moore SD, Schmidt BS, Klug M, Lipson M, Erickson D (2009) Optical manipulation of nanoparticles and biomolecules in sub-wavelength slot waveguides. *Nature* 457(7225):71–75

Publisher's Note Springer Nature remains neutral with regard to jurisdictional claims in published maps and institutional affiliations.

Affiliations

Farzan Akbaridoust¹  · Jimmy Philip¹ · David R. A. Hill² · Ivan Marusic¹

✉ Farzan Akbaridoust
farzan.akbaridoust@unimelb.edu.au

² Department of Chemical and Biomolecular Engineering,
University of Melbourne, Parkville, VIC 3010, Australia

¹ Department of Mechanical Engineering, University
of Melbourne, Parkville, VIC 3010, Australia